Research Article

Lanthanum-Based Perovskite-Type Oxides La$_{1-x}$Ce$_x$BO$_3$ (B = Mn and Co) as Catalysts: Synthesis and Characterization

Nyamdavaa Erdenee,[1] Uyanga Enkhnaran,[1,2] Sevjidsuren Galsan,[1] and Altantsog Pagvajav[1]

[1]*Institute of Physics and Technology, Mongolian Academy of Sciences, 13330 Ulaanbaatar, Mongolia*
[2]*Frank Laboratory of Neutron Physics, JINR, Dubna 141980, Russia*

Correspondence should be addressed to Nyamdavaa Erdenee; nyam_e@yahoo.com

La$_{1-x}$Ce$_x$CoO$_3$ (x = 0, 0.2, 0.4) and La$_{1-x}$Ce$_x$MnO$_3$ (x = 0, 0.2) perovskite-type oxides were prepared by sol-gel process. Characterization techniques EDS, FTIR, XRD, BET, and XPS experiments were performed to survey the composition, bulk structure, and the surface properties of perovskites. The reduction behavior, thermal stability, and catalytic activity were studied by H$_2$-TPR and catalytic performance. All synthesized samples showed well crystalline perovskite structure, 8–22 nm crystallite sizes, and SSA with 2–27 m^2 g^{-1}. The XRD results showed that the Ce substitution promoted the structural transformation for LaCoO$_3$ from rhombohedral into cubic and for LaMnO$_3$ no change in lattice geometry. Substitution with cerium (x = 0.2) showed smaller crystallite size, higher SSA, and the highest reducibility and catalytic activity for LaCoO$_3$.

1. Introduction

Lanthanum-based perovskite-type oxides with general formula ABO$_3$ (A = La^{3+}, Pr^{3+}, Nd^{3+}, etc.; A = Co^{3+}, Mn^{3+}, Sr^{3+}, etc.) may potentially replace noble metal catalysts due to their high catalytic activity, thermal stability, and low costs [1–3]. On the other hand, these materials present strong limitations for broader application in catalysis such as low surface area resulting from high calcination temperature and oxide instability at high operation temperature [4, 5]. Generally, an increase in the specific surface area of a perovskite-type oxide improves its catalytic activity by increasing the contact area between the catalyst and gas. Particles of perovskite-type oxides, which are the main factor of surface area, are still not small enough, largely because the conventional synthesis processes require calcination at high temperature. Thus, the obtained perovskite particles are heavily agglomerated and sintered, resulting in the low specific surface area [6, 7]. At present, a lot of efforts were carried out for the synthesis of perovskite with improved physical and chemical properties. LaBO$_3$ (B = Mn and Co) oxides have been evaluated with materials synthesized through methods such as pechini [8], sol-gel [9], citrate gel [10], and wet impregnation [5] methods.

Among these, the sol-gel method is one of the most effective for the synthesis of nanostructured perovskite-type oxides [11].

It has been reported that the ABO$_3$ perovskites can be properly modified by the partial substitution of atoms at A or B which dramatically enhance the activity and significant structural changes, such as lattice distortions, stabilization of multiple oxidation states, or generation of cationic and anionic vacancies. Many studies have reported that partial substitution at the A-site by a cation of different valence (e.g., La^{3+} by Ce^{4+} or Sr^{2+}) can form oxygen vacancies or change the oxidation state of the B-site cation, which enhances substantially the catalytic activity [12, 13]. Cerium is usually reported as a good promoter in perovskite lattice. An increase in the cerium substitution level up to 10% on the structure is expected to the enhancement in the activity that explained by oxygen excess in the lattice, cationic vacancies, structural defects, and the presence of multiple B oxidation states [14].

In this study, nanosized Ce-substituted perovskite-type oxides with x up to 0.4 were synthesized by sol-gel method and described structural change including Ce distribution. The prepared powder samples were systematically characterized by X-ray diffractometer (XRD), Fourier transform

infrared spectroscopy (FTIR), X-ray absorption spectroscopy (XAS), energy dispersive X-ray spectroscopy (EDS), and Brunauer-Emmett-Teller (BET) surface area analysis, X-ray photoelectron spectroscopy (XPS), and temperature-programmed reduction of H_2 (H_2-TPR). Catalytic activity and selectivity were examined on dehydrogenation propane reaction. Dehydrogenation of propane is attractive in terms of the direct conversion of economic feedstock, which can contribute to the future chemical industry. Perovskite catalysts possess high activities to propylene on this reaction [15].

Our results demonstrated that cerium substituted and nonsubstituted lanthanum-based perovskite-type oxides ($La_{1-x}Ce_xMnO_3$ and $La_{1-x}Ce_xCoO_3$) show promising structural, surface, electronic states and catalytic properties for catalyst application.

2. Experimental

2.1. Synthesis of the Perovskite. All $La_{1-x}Ce_xCoO_3$ and $La_{1-x}Ce_xMnO_3$ samples were prepared by the sol-gel method, which allows the formation of amorphous citrates of metals with a wide flexibility of compositions [16]. In our preparation procedure, the corresponding nitrates lanthanum (III) nitrate hexahydrate ($La(NO_3)_3 \cdot 6H_2O$) (Roth, 99.995%), cerium (III) nitrate hexahydrate ($Ce(NO_3)_3 \cdot 6H_2O$) (Aldrich, 99.95%), and cobalt (II) nitrate monohydrate ($Co(NO_3)_2 \cdot H_2O$) (Roth, 99.995%), and manganese (II) nitrate hexahydrate ($Mn(NO_3)_2 \cdot 6H_2O$) (Roth, 99.995%) in the appropriate quantities were dissolved in deionized water to give 0.1 M solutions. Citric acid monohydrate was added in 10 wt.% excess over the stoichiometric quantity to insure full complexation of the metal ions. Water was removed on a rotary evaporator at 80°C until the appearance of a gel. The obtained viscous material was dried overnight in a vacuum oven at 100°C. During this treatment, an intense production of nitrogen oxides occurred. The resulting strongly and highly hygroscopic and amorphous material was then crushed and calcined in air for 5 h at 750°C to obtain the desired phases.

2.2. Characterization. XRD data were obtained by using Maxima_X, XRD-7000 equipment with CuK_α radiation at room temperature. The structural parameters were determined by Rietveld analysis of the diffraction profiles. XAS measurements for Ce L_3, La L_3, and Co K-edges recorded at beam lines BL17C1 of National Synchrotron Center, Hsinchu, Taiwan. The data fitting was performed using the software package IFEFFIT. The specific surface areas were obtained by N_2 adsorption at 77 K, evaluated using the BET equation, on ASAP 2020. EDS elemental analysis was performed using an INCA system. The XPS data was obtained using a VG Scientific ESCALAB MKII spectrometer. The binding energy of the Au ($4f_{7/2}$) at 84.0 ± 0.1 eV was used to calibrate the binding energy scale of the spectrometer. XPS spectra smoothening and baseline subtraction were carried out using CasaXPS software. The experiments of the temperature-programmed reduction of H_2 (H_2-TPR) were carried out on Chem BET TPR/TPD Chemisorption Analyzer from Quantachrome.

TABLE 1: Weight percentages of the elements present in the samples obtained by EDS analysis.

Element	$La_{1-x}Ce_xCoO_3$		$La_{1-x}Ce_xMnO_3$	
	$x = 0$	$x = 0.2$	$x = 0$	$x = 0.2$
La	57.26 ± 0.39	50.84 ± 1.54	57.50 ± 2.39	47.77 ± 2.28
Co/Mn	27.22 ± 6.07	19.37 ± 1.01	18.46 ± 2.50	22.95 ± 0.13
O	15.52 ± 0.39	19.57 ± 0.12	24.05 ± 1.40	22.85 ± 1.09
Ce		9.22 ± 2.37		6.43 ± 1.06

2.3. Catalytic Activity Evaluation. Before the H_2-TPR experiment, the sample (ca. 0.10 g) was pretreated in an Ar stream at 150°C for 30 min and then cooled to room temperature. After that, a 5% H_2/Ar mixture stream was switched on and the temperature was increased at a rate of 10°C/min from room temperature to 900°C. The consumption of H_2 in the reactant stream was monitored with a thermal conductivity detector (TCD). The desorbed gases were monitored with a TCD and an online mass spectrometer (MS). The oxidative dehydrogenation of propane reaction was performed at atmospheric pressure in a fixed bed quartz reactor. For each testing, catalyst (ca. 0.20 g) was loaded in a quartz tubular reactor ($\Phi = 8$ mm). The remaining space of the reactor was filled with quartz sand to minimize possible homogeneous reaction [17]. Typical feed gases used were $V(C_3H_8) = 2$ mL min^{-1}, $V(O_2) = 2$ mL/min, and $V(N_2) = 16$ mL min^{-1} with a total flow rate of 20 mL min^{-1}. The reaction temperature was changed from 200 to 600°C at 25°C intervals. The highest temperature was consistent with the calcination temperature. The reaction products were analyzed on line by gas chromatography (GC) with a TCD detector using two packed columns, OV-1 column for CH_4, H_2, C_2H_4, C_3H_6, and C_3H_8 separation and TDX-01 column for O_2, CO, CO_2, and CH_4 separation.

3. Results and Discussion

3.1. Elemental Analysis. The elemental compositions of the $La_{1-x}Ce_xCoO_3$ and $La_{1-x}Ce_xMnO_3$ ($x = 0$, 0.2) perovskites determined by EDS analysis are summarized in Table 1. The EDS analysis shows the composition is almost the same (within experimental error) as the nominal composition of the samples.

3.2. FT-IR Spectra. As shown in Figure 1, synthesized $La_{1-x}Ce_xBO_3$ (B = Mn and Co) perovskites had vibration band around 600 cm^{-1}, which could be attributed to the characteristic absorption band of the stretching vibration of Co-O and Mn-O band of BO_6 octahedron. These strong absorption bands are indicating the formation of the perovskite-type structures and found to be shifted towards higher frequency with increases in Ce substitution concentration. Moreover, the intensity of this vibration band increases for $x = 0.2$ suggesting the change of oxidation state or oxygen vacancies. For the Ce-substituted $LaCoO_3$ perovskites, a peak observed at 663 cm^{-1} which can be related to the existence of cobalt cations into Co^{2+} and Co^{3+} valence states may be attributed to vibration of Co-O bonds in Co_3O_4 structure.
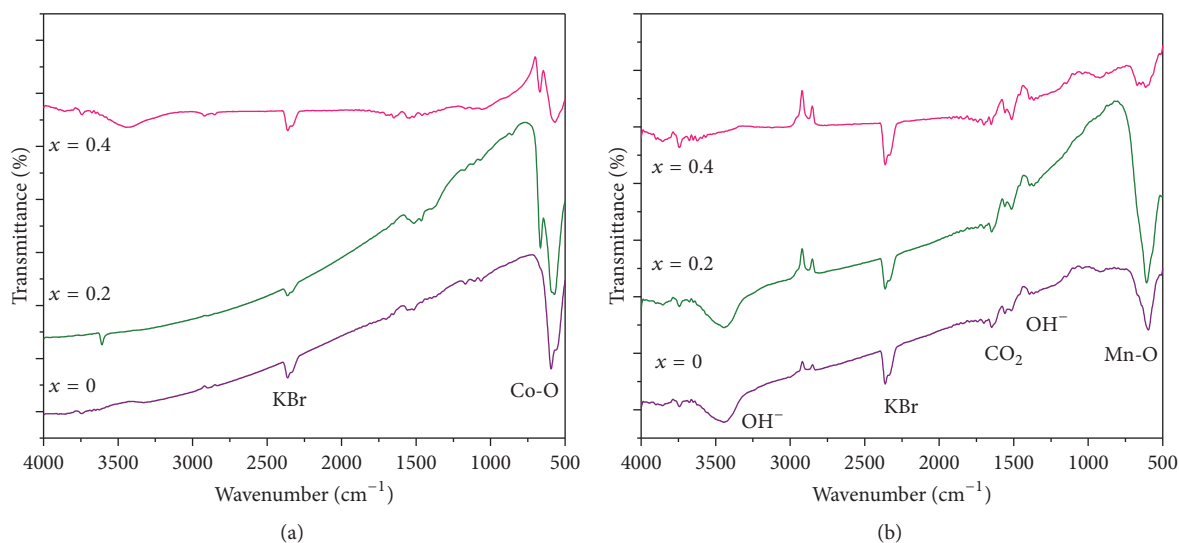
(a)

(b)

FIGURE 1: FT-IR spectra of the $La_{1-x}Ce_xCoO_3$ (a) and $La_{1-x}Ce_xMnO_3$ (b) perovskites (x = 0, 0.2, and 0.4). The most important vibration band around 600 cm^{-1} appears sharper for x = 0.2 suggesting the perovskite with more symmetrical structure.
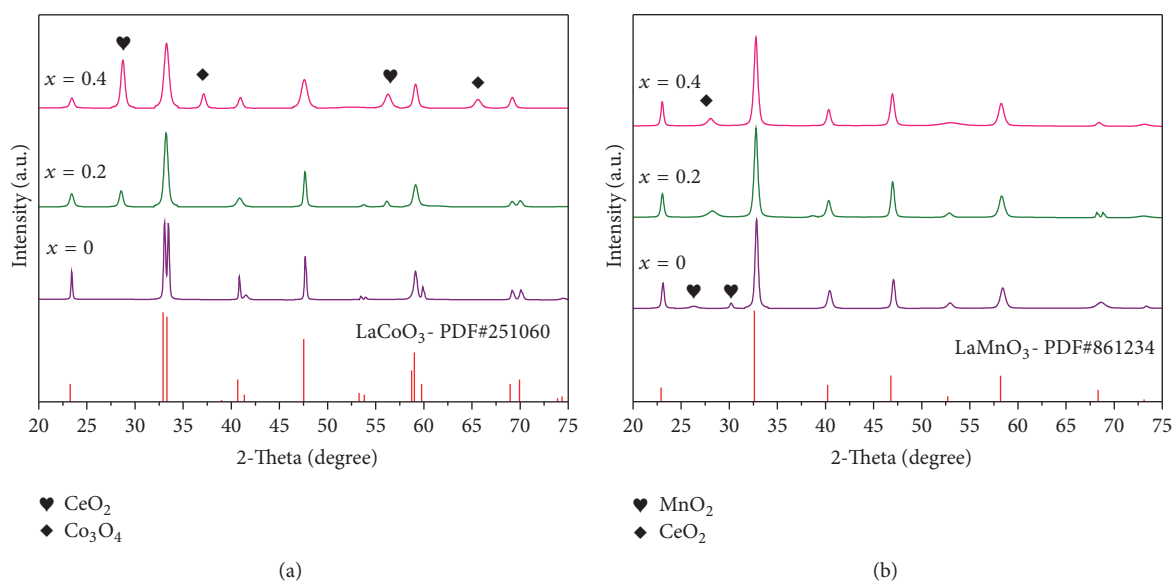

(a)

(b)

FIGURE 2: XRD patterns of the $La_{1-x}Ce_xCoO_3$ (a) and $La_{1-x}Ce_xMnO_3$ (b) perovskites (x = 0, 0.2, and 0.4). Additional CeO_2 phases were revealed for cerium substituted perovskites. The evolution of the CeO_2 peaks with increase in substitution is clearly seen.

The absorption peak at 2361 cm^{-1} and 1644 cm^{-1} is due to the deformation mode of absorbed molecular water of the carrier KBr(H$_2$O)n and CO$_2$, respectively [18, 19]. The broad band in the region of 3400 cm^{-1} and 1640 cm^{-1} is related to the H-O stretching and H-O-H bending vibration, which are associated with citrates and/or water molecules coordinated with the metal ions.

3.3. Structural Properties. Phase identification of the $La_{1-x}Ce_xCoO_3$ and $La_{1-x}Ce_xMnO_3$ (x = 0, 0.2 and 0.4) perovskites, based on the XRD results, is shown in Figure 2. Typical perovskite peaks for nonsubstituted samples are

well resolved with sharp and intense single peak in the pure LaCoO$_3$ and LaMnO$_3$ pattern [20]. Cerium substitution at higher levels (x > 0.15) cannot be incorporated into the lattice and leads to the formation of a separate CeO$_2$ phase (observed at 2θ = 28.6° and 56.5°). For x = 0, the structures were the rhombohedral LaCoO$_3$-type (JCPDS-ICDD 25-1060); when x = 0.2 and 0.4, the samples exhibited the pattern of cubic LaCoO$_3$ (JCPD-ICDD 75-0279). The peaks at 32.5° are found to merge single peak which indicates the transformation of structure from rhombohedral to cubic. This characteristic is a drastic indication for Ce substitution influence leading to a space group transformation into cubic

TABLE 2: XRD and BET analysis results of $La_{1-x}Ce_xCoO_3$ and $La_{1-x}Ce_xMnO_3$ ($x = 0$, 0.2, and 0.4) perovskites. Lattice parameters enlarged due to Ce substitution and the crystallite size decreased with the increase of substitution concentration.

| | Samples | | | | | |
| | $La_{1-x}Ce_xCoO_3$ | | | $La_{1-x}Ce_xMnO_3$ | | |
	$x = 0$	$x = 0.2$	$x = 0.4$	$x = 0$	$x = 0.2$	$x = 0.4$
Lattice parameter (Å)	$a = 5.401$, $c = 13.312$	$a = 5.379$	$a = 5.384$	$a = 5.501$, $c = 13.364$	$a = 5.497$, $c = 13.343$	$a = 5.507$, $c = 13.365$
Crystallite size (nm)	13.2	12.8	8.3	22.7	14.8	27.9
SSA (m^2g^{-1})	2.18	5.68	3.32	19.28	27.26	20.32

TABLE 3: XPS peak positions and atomic percentages of $La_{1-x}Ce_xCoO_3$ and $La_{1-x}Ce_xMnO_3$ perovskites obtained from the fitting of La 3d, Co 3p, Mn 3p, Ce 3d, and O1s XPS spectra.

	$LaCoO_3$	$La_{0.8}Ce_{0.2}CoO_3$	$La_{0.6}Ce_{0.4}CoO_3$	$LaMnO_3$	$La_{0.8}Ce_{0.2}MnO_3$
La 3d (eV)	834.3	834.7	834.3	834.7	834.4
	850.9	851.8	851.1	851.7	851.1
Co 3p/Mn 3p (eV)	779.9	780.2	779.9	641.8	641.8
	795.2	795.8	795.5	653.1	653.2
O 1s (eV)	528.5	528.8	528.7	528.8	528.9
	531.4	531.6	531.5	531.4	531.5
Ce[1] (at. %)	—	4.84 (3.9)	7.11 (3.6)	—	6.4 (10.1)
O (at. %)	75.1	73.6	73.4	77.4	74.9
La (at. %)	15.7	13.2	11.2	17.2	14.2

[1]The value in parenthesis is a peak percentage (%) of the Ce^{3+} ion.

lattice symmetry. When x is 0.4, characteristic peaks of the Co_3O_4 phase appeared around 37.1° and 56.4°. This conclusion confirms FTIR analysis result. The patterns of $LaMnO_3$ correspond to the rhombohedral perovskite-type (JCPDS-ICDD 86-1234) and the same lattice geometry observed in Ce-substituted perovskites [21–23]. The substitution $x = 0.4$, whose peak in the inset is not as sharp as that for the case $x = 0.2$, and more unreacted CeO_2 aggregates appear.

Therefore, its intensity increases with the addition of cerium due to solubility limit mentioned in the introduction section. The peaks between 32 and 33° indicate that augmentation of Ce concentration leads to broadening and peak shifts in the XRD pattern due to changes or distortions of the cell lattice.

Table 2 summarizes the crystallite size, the BET specific surface area, and lattice parameters of all samples. The average crystallite size (D) was determined using Debye-Scherrer's equation $D = 0.9\lambda/\beta \cos\theta$, where λ is the incident X-ray wavelength ($\lambda_{Cu} = 1.5443$ Å), β is full width at half maximum (FWHM) of the peak corresponding to maximum intensity, and θ represents the diffraction angle of the most intense peak in degrees. The crystallite size of the samples was found to be in the range of 13 to 8 nm for $La_{1-x}Ce_xCoO_3$ and relatively larger 22–14 nm for $La_{1-x}Ce_xMnO_3$ which decreases with Ce content augmentation. That should be expected since the higher Ce^{4+} coordination with their surrounding oxygen atoms (within the same crystal plane) than trivalent La^{3+} tends to inhibit crystal growth, resulting in smaller crystal size [24]. Therefore, the crystallite size was increased in $La_{0.6}Ce_{0.4}MnO_3$ perovskite due to Ce segregation.

3.4. Specific Surface Area.

$La_{1-x}Ce_xMnO_3$ perovskites showed higher specific surface areas (SSA) than $La_{1-x}Ce_xCoO_3$ which are 19–27 m^2/g and 2–5 m^2/g, respectively (Table 2). Calcination at high temperature is necessary to obtain the perovskite-type oxides, but such treatment often results in a dramatic decrease in the specific surface area ($LaMnO_3 < 30$ m^2/g and $LaCoO_3 < 10$ m^2/g). Generally, the substituted samples have a larger SSA than pure perovskites and the enhancement was not linear with the substitution. When cerium addition was 0.2, a significant increase in SSA appeared, when $x = 0.4$, with the increased proportion of additional phases (CeO_2) as shown in XRD profiles and their SSA decreased.

The particle size obtained by XRD and BET can be compared to get the information about agglomeration. If defining $\varphi = D_{BET}/D_{XRD}$ as a factor to reflect the agglomeration extent of the primary crystalline, φ value of 1.0 indicates no agglomeration [25]. In this work, agglomeration factors were 2.8, 1.57, and 1.38 for $La_{1-x}Ce_xCoO_3$ with $x = 0$, 0.2 and 0.4, respectively. These results suggest that our synthesized perovskites have agglomeration. However, agglomeration factors of $La_{1-x}Ce_xCoO_3$ show better results compared to $La_{1-x}Ce_xMnO_3$ perovskites ($\varphi = 1.9$, 2.15, and 1.53 for $x = 0$, 0.2, and 0.4, resp.).

3.5. Surface Analysis.

The surface compositions of perovskites were studied by XPS. Any charging shift produced in the spectrum by the sample was corrected by taking C 1s position (284.6 eV) as a reference line. Table 3 lists the corresponding binding energies of La 3d, O 1s, Ce 3d, Co 2p, and Mn 2p of $La_{1-x}Ce_xCoO_3$ and $La_{1-x}Ce_xMnO_3$ perovskite

(a)

(b)

(c)

(d)
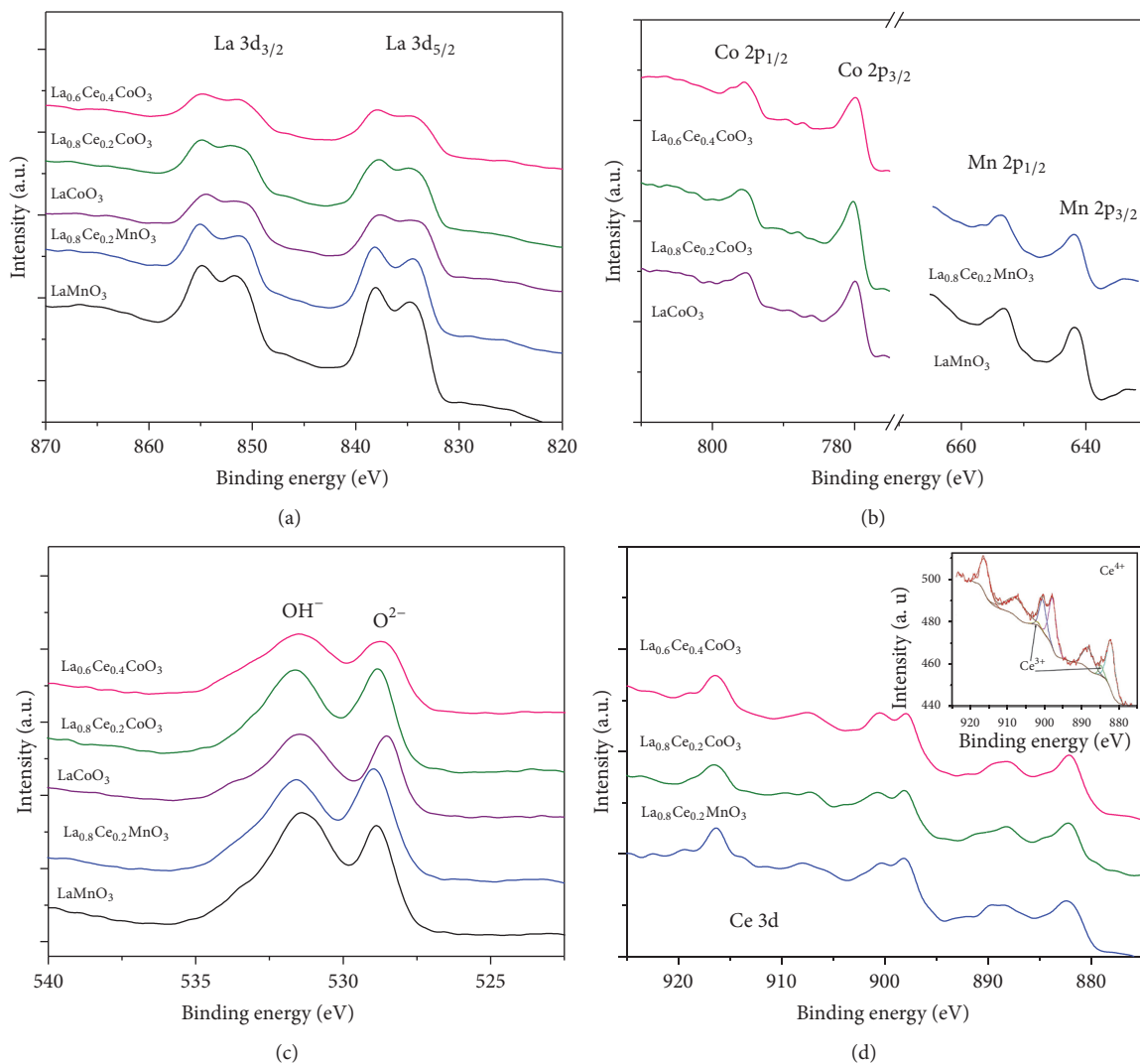
FIGURE 3: La 3d (a), Co and Mn 2p (b), O 1s (c), and Ce 3d (d) core level XPS spectra of $La_{1-x}Ce_xCoO_3$ and $La_{1-x}Ce_xMnO_3$ (x = 0, 0.2, and 0.4) perovskites.

(x = 0, 0.2, and 0.4) samples. The binding energy values of La 3d were recorded around 834 and 851 eV. The other two peaks at 837 and 854 eV are La 3d satellite peaks. These peak positions are similar to the values recorded from pure La_2O_3 [26], indicating that La ions were in a trivalent state. Moreover, the La $3d_{5/2}$ and La $3d_{3/2}$ peaks shifted to higher energy for of $La_{0.8}Ce_{0.2}CoO_3$, which probably connected with different chemical surroundings (Figure 3(a)). Co 2p peaks were occupied at approximately 779.9 eV which indicates Co^{3+} is dominant in of $La_{1-x}Ce_xCoO_3$ perovskites. When x = 0.2, the peak shifted to 780.3 eV that reveals the increasing of Co^{2+} ion content and besides the peak shifted back at x = 0.4. According to the XRD results, no Co_3O_4 phase was observed in x = 0.2 perovskite. These findings indicate that Ce^{4+} substitution created Co have lower oxidation states as a charge compensation mechanism. The peaks of Mn $2p_{3/2}$ and Mn $2p_{1/2}$ are located at 641.8 and 653.1 eV and assigned to Mn^{3+} ions. Moreover, no peak shift was observed for $La_{0.8}Ce_{0.2}MnO_3$.

Figure 3(c) shows the O 1s core-level spectra of perovskites. The peak at 530.9 eV for the perovskite is due to O^{2-} ions in the lattice and the peak at 532.7 eV can be attributed to adsorbed oxygen such as OH^- whereas adsorbed molecular water was at above 533.2 eV. The adsorbed oxygen decreased at x = 0.2 and 0.4 in which proposing cation vacancy defects could be generated as the substitution of Ce ions of perovskites. The ratio of adsorbed and lattice oxygen decreased at x = 0.2 of all perovskites which are believed to support reducible oxide structure [27]. XPS spectra of Ce 3d are shown in Figure 3(d). Six different characteristic peaks are indexed to Ce^{4+} and presence of Ce^{3+} ions (inset graph of Figure 3(d)) can also be revealed in perovskites. The Ce^{4+} and Ce^{3+} atomic percentages have been obtained from the area of the peaks by the CasaXPS fitting program (Table 3).

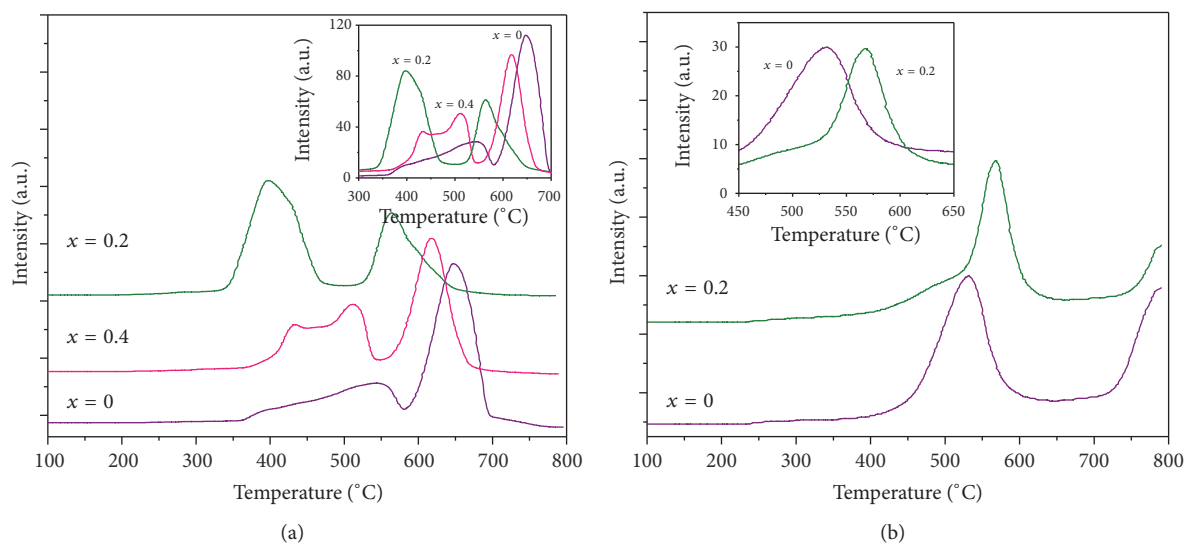3.6. Temperature-Programmed Reduction. Temperature-programmed reduction profile of $La_{1-x}Ce_xCoO_3$ and

FIGURE 4: H_2-TPR profiles of $La_{1-x}Ce_xCoO_3$ (a) and $La_{1-x}Ce_xMnO_3$ (b) perovskites (x = 0, 0.2, and 0.4). The reduction peaks shifted to the lower temperature, indicating that Ce^{4+} insertion increased the catalyst reducibility.

TABLE 4: H_2 consumed for the first step and second step of reduction on $La_{1-x}Ce_xCoO_3$ and $La_{1-x}Ce_xMnO_3$ (x = 0, 0.2, and 0.4) perovskite catalysts.

Catalyst composition	First step of reduction	Reduction temperature (°C)	Second step of reduction	Reduction temperature (°C)
$LaCoO_3$		391 (surface) 548 (bulk)		648
$La_{0.8}Ce_{0.2}CoO_3$	Co^{3+} to Co^{2+}	413	Co^{2+} to Co^0	575
$La_{0.6}Ce_{0.4}CoO_3$		427 (surface) 508 (bulk)		616
$LaMnO_3$	Mn^{4+} to Mn^{3+}	542	Mn^{3+} to Mn^{2+}	798
$La_{0.8}Ce_{0.2}MnO_3$	Mn^{4+} to Mn^{3+}	571	Mn^{3+} to Mn^{2+}	798

$La_{1-x}Ce_xMnO_3$ perovskites are shown in Figure 4. All of the TPR patterns of perovskites including sharp peaks suggest that well-defined crystalline structure is formed. Royer et al. [28] reported two successive steps in TPR profile of $LaCoO_3$ perovskite. The first reduction step occurs at low temperature (<500°C) which reduces Co^{3+} into Co^{2+}. The second reduction step (reduction of the Co^{2+} into Co^0) starts at the temperature higher than 600°C. Since La^{3+} was nonreducible under the conditions of H_2-TPR, the observed H_2 consumption peaks in the TPR profile of $LaCoO_3$ were due to the reduction of Co^{n+} cation only.

As seen from H_2-TPR profile (Figure 4(a)), the H_2 consumption provides evidence for the complete reduction of Co^{3+} to Co^0 occurring in two steps from Co^{3+} to Co^{2+} with a peak at about 400°C and Co^{2+} to Co^0 centered at about 600°C in agreement with the literature [28]. For $La_{0.6}Ce_{0.4}CoO_3$ perovskite, three reduction peaks were detected which suggest a multiple-step reduction (Table 4). Compared with the pure $LaCoO_3$ and $LaMnO_3$ perovskites, the two reduction peaks of the Ce-substituted samples all shift to lower temperature direction correspondingly. And x = 0.2 substitution leads to the highest decrease in the reduction peak temperatures and creates an easier reducibility of the Co^{3+} into Co^{2+}. The H_2-TPR results supported XPS analysis by showing that cerium substitution increased the reducibility, especially at

the temperature range of 300–550°C, suggesting that Ce^{4+} increased the number of cation vacancies within the lattice.

Figure 1(b) shows the H_2-TPR profile of $La_{1-x}Ce_xMnO_3$ perovskite catalysts. H_2 consumption provides evidence for the reduction of Mn^{4+} to Mn^{2+} occurring in two steps from Mn^{4+} to Mn^{3+} with a peak maximum at 542°C and reduction of Mn^{3+} to Mn^{2+} at 798°C. For $La_{0.8}Ce_{0.2}MnO_3$ perovskite catalyst, first peak at 571°C and the second peak at 798°C were observed (Table 4). The Ce^{4+} insertion decreased the catalyst reducibility of Mn^{4+} to Mn^{3+} for $LaMnO_3$ perovskite, shifting reduction peaks to the higher temperature. But cerium has less influence on the reduction of Mn^{3+} to Mn^{2+}. This indicates that the Mn is reduced to +3 during cerium substitution [29]. Based on the H_2-TPR results, it is indicated that the $La_{1-x}Ce_xCoO_3$ showed higher reducibility (inset of Figure 4) than $La_{1-x}Ce_xMnO_3$ which was beneficial for catalyst application.

3.7. Catalytic Activity. The values of propane conversion and selectivity as a function of reaction temperature are shown in Figure 5. It can be seen that all Ce-substituted catalysts have better activity than the pure perovskite. Pure $LaCoO_3$, as prepared in this work as reference, exhibited very low activity (37.7% conversion and 78.8% selectivity at 500°C). In the case of perovskite samples, ever since the addition of cerium,
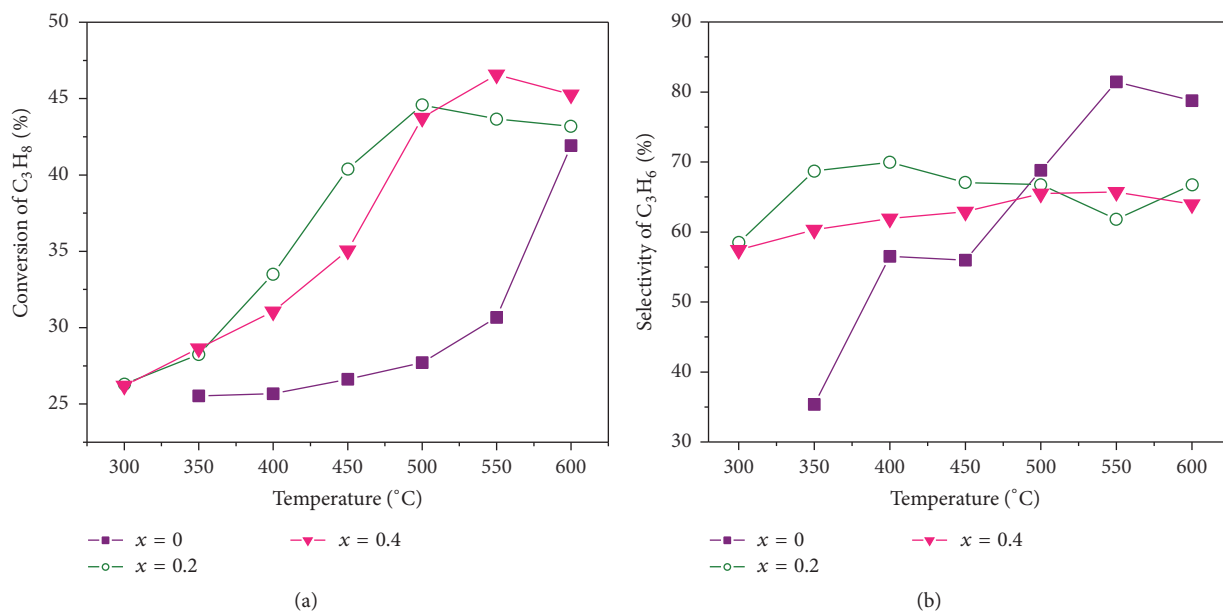
FIGURE 5: Conversion of propone (a) and selectivity (b) as a function of the temperature of reaction for catalysts $La_{1-x}Ce_xCoO_3$ ($x = 0$, 0.2, and 0.4).

the large enhancement of the activity for dehydrogenation of propane was observed and the maximum activity point moved to the lower temperature.

The sample with $La_{1-x}Ce_xCoO_3$ ($x = 0.2$) gives the best catalytic performance, about 54.6% conversion and 76.8% selectivity at 500°C. When x is 0.4, conversion of 53.7% and selectivity of 75.3% were obtained at the same temperature. At temperatures higher than 500°C, Co^{n+} species coexist with metallic Co^0 (supported by H_2-TPR experiment) which leads to undesirable methanation reaction [15, 30]. Compared with the perovskite-type oxides, the activity of pure Co_3O_4 was low, and CeO_2 did not even show any activity for dehydrogenation of propane which is not mentioned in these figures. Thus, the additional phases would not contribute much to the catalytic activity directly [13]. Consequently, the $La_{0.8}Ce_{0.2}CoO_3$ catalyst shows the highest activity and selectivity to propylene on dehydrogenation of propane.

4. Conclusion

In this work, lanthanum-based perovskite-type oxides $La_{1-x}Ce_xBO_3$ (B = Mn and Co, $x = 0$, 0.2, and 0.4) were successfully synthesized by sol-gel method and investigated as a catalyst. Structural investigations indicated that $La_{1-x}Ce_xMnO_3$ had a single perovskite structure of rhombohedral and $La_{1-x}Ce_xCoO_3$ exhibited a transformation in the phase structure (from rhombohedral to the cubic) with increasing cerium content. The estimated optimal average crystallite size is found to be less than 15 nm for both samples. BET results showed an increase (not linear) in the specific surface area upon Ce content. The catalytic activities in the dehydrogenation of propane were enhanced significantly

with Ce substitution and achieved the best when x was 0.2 but decreased at 0.4. The cerium substitution when $x = 0.2$ leads to an increase of cation vacancies as charge compensation mechanism and results in enhancement of the catalytic activity, the reducibility, and the selectivity.

Among these catalysts, $La_{0.8}Ce_{0.2}CoO_3$ catalyst shows best performances with high catalytic activity, selectivity, and stability, suggesting that it may a promising candidate for the catalyst applications. $La_{1-x}Ce_xMnO_3$ ($x = 0$, 0.2) perovskites with rhombohedral structure show the poorest reducibility as well as the highest specific surface areas. In addition, since we confirmed that the present sol-gel method can be used for perovskite-type oxides with different compositions, it may be useful for SOFC catalyst materials.

Conflicts of Interest

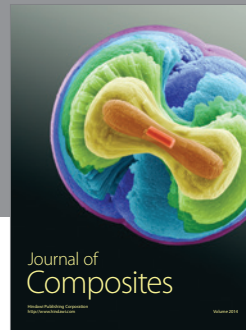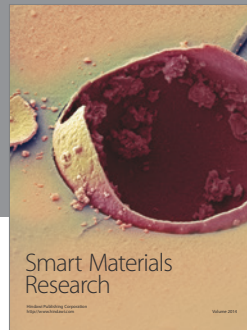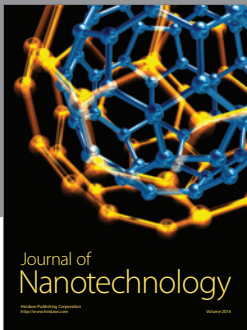The authors declare that they have no conflicts of interest.

Acknowledgments

References

[1] J. Dukić, S. Bošković, and B. Matović, "Crystal structure of Ce-doped CaMnO$_3$ perovskite," *Ceramics International*, vol. 35, no. 2, pp. 787–790, 2009.

[2] S. T. Fabio and S. Martin, "Improvement of catalytic performance of perovskites by partial substitution of cations and supporting on high surface area materials," in *Perovskite Materials-Synthesis, Characterisation, Properties, and Applications*, InTechOpen, Rijeka, Croatia, 2016.

[3] T. Nagai, N. Fujiwara, M. Asahi, S. Yamazaki, Z. Siroma, and T. Ioroi, "Synthesis of nano-sized perovskite-type oxide with the use of polyvinyl pyrrolidone," *Journal of Asian Ceramic Societies*, vol. 2, pp. 329–332, 2014.

[4] J. Kirchnerova, M. Alifanti, and B. Delmon, "Evidence of phase cooperation in the $LaCoO_3$–CeO_2–Co_3O_4 catalytic system in relation to activity in methane combustion," *Applied Catalysis A: General*, vol. 231, no. 1-2, pp. 65–80, 2002.

[5] L. Predoana, B. Malic, and M. Zaharescu, "$LaCoO_3$ formation from precursors obtained by water-based sol-gel method with citric acid," *Journal of Thermal Analysis and Calorimetry*, vol. 98, no. 2, pp. 361–366, 2009.

[6] Z. Chendong, L. Mingfei, and L. Meilin, "Sol- gel processing for Conventional and Alternative Energy," in *Advances in Sol-Gel Derived Materials and Technologies*, 2012.

[7] K. Li, R. Cheng, S. Wang, and Y. Zhang, "Infrared transmittance spectra of the granular perovskite $La_{2/3}Ca_{1/3}MnO_3$," *Journal of Physics: Condensed Matter*, vol. 10, no. 19, pp. 4315–4320, 1998.

[8] E. Nyamdavaa, P. Altantsog, E. Uyanga et al., "Crystal structure study of Perovskite-type $LaCoO_3$ electro-catalyst synthesized by Pechini method," in *Proceedings of the 6th International Forum on Strategic Technology (IFOST '11)*, pp. 61–64, August 2011.

[9] M. A. Peca and J. L. G. Fierro, "Chemical structures and performance of perovskite oxide," *Chemical Reviews*, vol. 101, no. 7, pp. 1981–2017, 2001.

[10] C. Olive, L. Forni, A. Ambrosio, F. Navarrini, and A. D. Stepanov, "Characterization by EPR and other techniques of $La_{1−x}Ce_xCoO_{3+\delta}$ perovskite-like catalysts for methane flameless combustion," *Applied Catalysis A*, vol. 205, pp. 245–252, 2001.

[11] Y. Wen, C. Zhang, H. He, Y. Yu, and Y. Teraoka, "Catalytic oxidation of nitrogen monoxide over $La_{1−x}Ce_xCoO_3$ perovskites," *Catalysis Today*, vol. 126, no. 3-4, pp. 400–405, 2007.

[12] J. Feng, T. Liu, Y. Xu, J. Zhao, and Y. He, "Low-temperature preparation of lanthanum-doped $BiFeO_3$ crystallites by a sol–gel-hydrothermal method," *Ceramics International*, vol. 37, no. 7, pp. 2359–2364, 2011.

[13] Y. Wen, C. Zhang, H. He, Y. Yu, and Y. Teraoka, "Catalytic oxidation of nitrogen monoxide over $La_{1−x}Ce_xCoO_3$ perovskites," *Catalysis Today*, vol. 126, no. 3-4, pp. 400–405, 2007.

[14] H. Taguchi, S. Yamasaki, A. Itadani, M. Yosinaga, and K. Hirota, "CO oxidation on perovskite-type $LaCoO_3$ synthesized using ethylene glycol and citric acid," *Catalysis Communications*, vol. 9, no. 9, pp. 1913–1915, 2008.

[15] R. Watanabe, Y. Hondo, K. Mukawa, C. Fukuhara, E. Kikuchi, and Y. Sekine, "Stable and selective perovskite catalyst for dehydrogenation of propane working with redox mechanism," *Journal of Molecular Catalysis A: Chemical*, vol. 377, pp. 74–84, 2013.

[16] E. Nyamdavaa, E. Uyanga, G. Sevjidsuren, and P. Altantsog, "Preparation and characterization of $La_{1−x}Ce_xCoO_3$ perovskite oxides for energy materials," in *Proceedings of the 50th School on Condensed Matter Physics*, E14-2016-24, p. 144, Joint Institute for Nuclear Research, Saint-Petersburg, Russia, 2016.

[17] A. Mishra and R. Prasad, "Effect of preparation method and calcination temperature on $LaCoO_3$ perovskite catalyst for diesel soot oxidation," *Canadian Chemical Transactions*, vol. 3, no. 1, pp. 95–107, 2015.

[18] M.-J. Lee, J.-H. Jun, J.-S. Jung, Y.-R. Kim, and S.-H. Lee, "Catalytic activities of perovskite-type $LaBO_3$ (B = Fe, Co, Ni) oxides for partial oxidation of methane," *Bulletin of the Korean Chemical Society*, vol. 26, no. 10, pp. 1591–1596, 2005.

[19] A. E. Hernandez, V. Sagredoa, and G. H. Delgadob, "Synthesis and magnetic characterization of $LaMnO_3$ nanoparticles," *Revista Mexicana de Física*, vol. 61, pp. 166–169, 2015.

[20] T. T. Nguyen, T. T. Ngo, and K. Serge, "Characteristics and reducibility of nanosized $La_{1−x}Ce_xCoO_3$ perovskites synthesized by reactive grinding," *Journal of Chemistry*, vol. 47, no. 5, pp. 552–557, 2009.

[21] W. J. Kuen, L. K. Pah, A. H. Shaari, C. S. Kien, N. S. Wei, and A. G. H. Ming, "Effect of rare earth elements substitution in La site for $LaMnO_3$ manganites," *Pertanika Journal of Science and Technology*, vol. 20, no. 1, pp. 81–88, 2012.

[22] C. Zhang, W. Hua, C. Wang et al., "The effect of A-site substitution by Sr, Mg and Ce on the catalytic performance of $LaMnO_3$ catalysts for the oxidation of vinyl chloride emission," *Applied Catalysis B: Environmental*, vol. 134-135, pp. 310–315, 2013.

[23] A. R. Shelke and N. G. Deshpande, "Influence of the calcination temperature on the combustion synthesized perovskite $LaMnO_3$ compound," *Journal of Nano- and Electronic Physics*, vol. 7, no. 3, pp. 03009–03015, 2015.

[24] G. Pecchi, R. Morales, E. J. Delgado, R. Jimenez, and M. Fraga, "Catalytic combustion of soot on Ce-doped lanthanum cobaltites," *Journal of the Chilean Chemical Society*, vol. 59, no. 4, pp. 2725–2730, 2015.

[25] D. Ding, B. Liu, Z. Zhu, Sh. Zhou, and Ch. Xia, "High reactive $Ce_{0.8}Sm_{0.2}O_{1.9}$ powders via a carbonate co-precipitation method as electrolytes for low-temperature solid oxide fuel cells," *Solid State Ionics*, vol. 179, no. 21–26, pp. 896–899, 2008.

[26] J. Zhu, Y. Zhao, D. Tang, Z. Zhao, and S. A. C. Carabineiro, "Aerobic selective oxidation of alcohols using $La_{1−x}Ce_xCoO_3$ perovskite catalysts," *Journal of Catalysis*, vol. 340, pp. 41–48, 2016.

[27] G. T. Tan, S. Y. Dai, P. Duan, Y. L. Zhou, H. B. Lu, and Z. H. Chen, "Structural, electric and magnetic properties of the electron-doped manganese oxide: $La_{1−x}Te_xMnO_3$ (x = 0.1, 0.15)," *Journal of Applied Physics*, vol. 93, no. 9, article 5480, 2003.

[28] E. Royer, J. Chauvel, V. Courboulay, R. Granier, and J. Albar, "Grain legumes, rapeseed meal and oil seeds for weaned piglets and growing/finishing pigs," *Techni-Porc*, vol. 28, pp. 13–19, 2005.

[29] Y. Zhang-Steenwinkel, J. Beckers, and A. Bliek, "Surface properties and catalytic performance in CO oxidation of cerium substituted lanthanum-manganese oxides," *Applied Catalysis A: General*, vol. 235, no. 1-2, pp. 79–92, 2002.

[30] C. L. Pieck, M. A. Bañares, and J. L. G. Fierro, "Propane oxidative dehydrogenation on VO_x/ZrO_2 catalysts," *Journal of Catalysis*, vol. 224, no. 1, pp. 1–7, 2004.